nature catalysis

Article

https://doi.org/10.1038/s41929-025-01449-9

Local solid-state processes adjust the selectivity in catalytic oxidation reactions on cobalt oxides

Received: 12 July 2024

Accepted: 21 October 2025

Published online: 18 November 2025

Check for updates

Thomas Götsch[1] ✉, Daniel Cruz[1], Patrick Zeller[1,2], Anna Rabe[3,4], Maik Dreyer[4], Nicolas Cosanne[3], Frank Girgsdies[1], Jasmin Allan[1], Michael Hävecker[1,5], Anna Efimenko[6,7], Mihaela Gorgoi[6,7], Sharif Najafishirtari[3], Malte Behrens[3,4], Robert Schlögl[1,5], Axel Knop-Gericke[1,5] & Thomas Lunkenbein[1,8,9] ✉

Transition metal oxides are excellent catalysts for selective oxidation reactions, which are a prominent source of industrially relevant chemicals. However, these reactions suffer from multiple competing reaction pathways, limiting the selectivity. Thus, it is essential to gain an understanding of the underlying processes occurring on the catalyst that affect its performance. Here we synergistically combine operando X-ray spectroscopy and operando transmission electron microscopy to unravel a network of solid-state processes that controls the catalytic properties of Co_3O_4 in the oxidation of 2-propanol towards acetone. These include exsolution, diffusion and defect formation, which strongly distort the catalyst lattice at lower temperatures. Ultimately, they also lead to a maximum in acetone selectivity when the catalyst is trapped in a frustrated or metastable state at the onset of crystallization of the exsolved particles to CoO and void formation, which coincides with the maximum in surface cobalt oxidation state in the spinel.

One of the key parameters of catalytic conversion is the selectivity towards the desired product[1], eliminating the need for expensive product purification steps. This is especially important in reactions that can lead to a multitude of different products, such as (selective) alcohol oxidation[2], which is one of the most prominent heterogeneously catalysed industrial processes, used in the production of fundamental chemicals such as formaldehyde or acetone[3]. The latter can be obtained by oxidation of 2-propanol, the main reactions of which are presented in Fig. 1a: dehydration of 2-propanol leads to the formation of propene, whereas dehydrogenation and oxidative dehydrogenation both yield acetone[4,5]. At higher temperatures, total oxidation becomes predominant. These reactions are typically catalysed by transition metal oxides[2], where the cobalt spinel oxide (Co_3O_4) has shown to be a promising candidate for a variety of oxidation reactions[4,6–10].

Understanding the full details of such heterogeneously catalysed processes requires operando techniques. These analytical methods, applied under reaction conditions while simultaneously monitoring the activity of the catalytic system[11,12], are essential for observing the evolution of the catalyst and identifying active and selective phases. During its exposure to thermal and chemical stimuli, reversible processes and metastable states of the catalyst can be witnessed that would otherwise be missed in ex situ investigations. This includes phase transitions and solid-state diffusion phenomena that can substantially alter the catalytic performance, such as restructuring[13,14], dissolution of reaction intermediates such as carbon[15], or strong metal–support interactions[16].

In this work, we present a combined operando investigation to demonstrate that a complex network of bulk and surface solid-state processes dominates the selective gas-phase oxidation of 2-propanol

A full list of affiliations appears at the end of the paper. ✉e-mail: goetsch@fhi-berlin.mpg.de; lunkenbein@fhi-berlin.mpg.de

https://doi.org/10.1038/s41929-025-01449-9

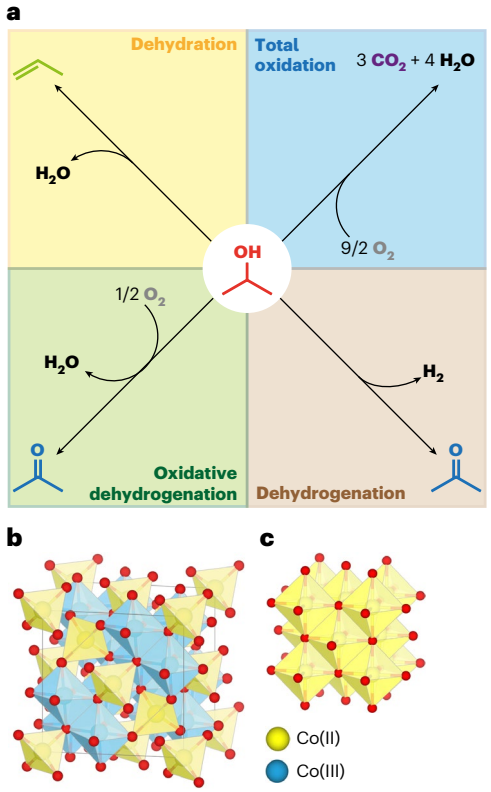

Fig. 1 | Reaction pathways and crystal structures. a, Overview of the four main reaction pathways in the oxidation or dehydration of 2-propanol. **b**, Crystal structure of the spinel oxide, Co_3O_4. Tetrahedrally coordinated Co(II) species are yellow; Co(III), in distorted octahedra, are blue. **c**, Rock-salt-structured CoO, with octahedrally coordinated Co(II) ions.

on unsupported Co_3O_4 catalysts (hydroxide-derived hexagonal platelets). By combining synchrotron-based (operando) near-ambient pressure X-ray photoelectron spectroscopy (NAP-XPS) and near-edge X-ray absorption fine structure spectroscopy (NEXAFS) with operando transmission electron microscopy (OTEM) on the same catalyst, a thorough understanding of the catalyst behaviour can be obtained: while the X-ray spectroscopy techniques, yielding information on the electronic structure, excel in their surface sensitivity and high energy resolution, OTEM allows the direct visualization of the morphological and atomic/crystallographic structure of the catalyst and gives rise to spatially resolved information[17], revealing that the reaction is strongly influenced by diffusional processes such as exsolution, crystallization and vacancy collapse.

Results

Activity

Phase-pure anisotropic hexagonal platelets of cobalt(II, III) oxide (Co_3O_4) have been used as a catalyst in the selective oxidation of 2-propanol (see Supplementary Figs. 1–4 for the general characterization of the catalyst). Figure 1b displays the crystal structure of Co_3O_4 which is comprised of octahedrally coordinated Co(III) (blue) and tetrahedrally coordinated Co(II) ions (yellow)[18,19]. CoO, on the other hand (Fig. 1c), consists of octahedrally coordinated Co(II) ions[20], featuring the same oxygen sublattice as the spinel, but with different cation lattices[21]. As outlined in Supplementary Fig. 5, all operando experiments followed the same procedure: in a first calcination step, the sample is preoxidized at 600 °C in oxygen, followed by two subsequent catalytic runs (2-propanol/O_2 1:1, Supplementary Table 1) in various temperature steps up to a maximum of 300 °C. Before the third run, the sample is reoxidized using the same conditions as for the precalcination.

Activity data from a fixed-bed reactor (Fig. 2a, following the procedure given above and in Supplementary Fig. 5) agrees qualitatively with the data obtained from both operando experiments (see Fig. 2b,c for NAP-XPS and OTEM, respectively; see Methods section for experimental details, and Supplementary Figs. 7 and 8, and Supplementary Note 1). In all cases, conversion is detectable, even in OTEM despite the low catalyst loadings. As expected, the more basic surface of Co_3O_4 favours acetone over propene[22,23]. The catalytic activity shown in Fig. 2 can generally be split into two regimes: a low-temperature region below 200 °C, where the catalyst deactivates rapidly and no stable conversion is attainable (see also Supplementary Note 2 for an analysis of the spikes), and a high-temperature regime above 200 °C with stable conversion, as described by Anke et al.[4] After reaching the high-temperature regime, the low-temperature activity is inhibited completely in the second run and can only be recovered in the third run after reoxidation of the system. Afterwards, the low-temperature regime reappears in the third run. However, even the high-temperature region seems to feature two pathways based on the extracted activation energies (Fig. 2d and Supplementary Figs. 9 and 10). The activation energy of the first pathway in the high-temperature regime (between 200 and 250 °C) changes significantly between the first and second run, suggesting that the changes to the catalyst not only affect the low-temperature regime but also the high-temperature one. Note that individual reactants and products have different apparent activation energies because they participate in separate sets of reactions with different apparent activation energies (Fig. 1a and Supplementary Note 3, including Supplementary Figs. 12 and 15).

Electronic structure

From the NAP-XPS cobalt 2*p* spectra, the intensity ratios between the contributions of Co(III) (binding energy, 779.6 eV) and Co(II) (780.4 eV)[24] to the cobalt $2p_{3/2}$ peak can be extracted as a measure of the oxidation state for different kinetic energies, corresponding to different signal depths (Fig. 3a; see also Supplementary Figs. 18–24, and Supplementary Note 5, including Supplementary Table 4 for the spectra and estimates of these depths).

The surface oxidation state (signal depth, 0.6 nm) exhibits a parabolic temperature dependency, reaching a maximum at 200 °C, the same temperature at which the conversion becomes stable (Fig. 2). At room temperature, both surface and subsurface (signal depth, ~1.3 nm) cobalt are strongly reduced; however, in the subsurface spectra, the oxidation state increases drastically up to 100 °C, followed by a slight linear decrease. The bulk-sensitive measurement (bottom, signal coming from the outermost 4.8 nm) shows no clear trend within the error, with data points scattering very close to the value obtained during preoxidation (blue dashed line), suggesting that changes are limited to the surface-near regions, which is in agreement with cobalt K-edge XANES (Supplementary Note 7). Similar behaviours are observed in the second and third catalytic runs, and are confirmed by an analogous analysis of the cobalt $2p_{3/2}$ satellites (Supplementary Figs. 22 and 23). The strong reduction observed at room temperature also causes substantial charging (which is not observed in any other conditions and has been corrected for; Methods), implying that the reduction leads to an increase of the bandgap, which is in agreement with the typical assignment of this (direct) transition (~1.65 eV) to a Co(III) → Co(II) charge transfer[25,26].

Next, the cobalt L_3 edges of Co_3O_4 (Supplementary Figs. 25–27) contain signatures of octahedrally coordinated Co(III) (780.3 eV), tetrahedrally coordinated Co(II) (778.6 eV) and Co(II) in octahedral configuration (777.3 eV)[27], which allow for a more differentiated analysis (Fig. 3b, surface-sensitive Auger electron yield (AEY)): at room temperature, there is an accumulation of Co^{II}_{tet}, and to an even larger degree of Co^{II}_{oct}. All intensity ratios in Fig. 3b seem to evolve parabolically with temperature, although the maximum of $Co^{III}_{oct}/Co^{II}_{tet}$ occurs at as low as ~150 °C. Indeed, especially in the subsurface-sensitive total electron

https://doi.org/10.1038/s41929-025-01449-9

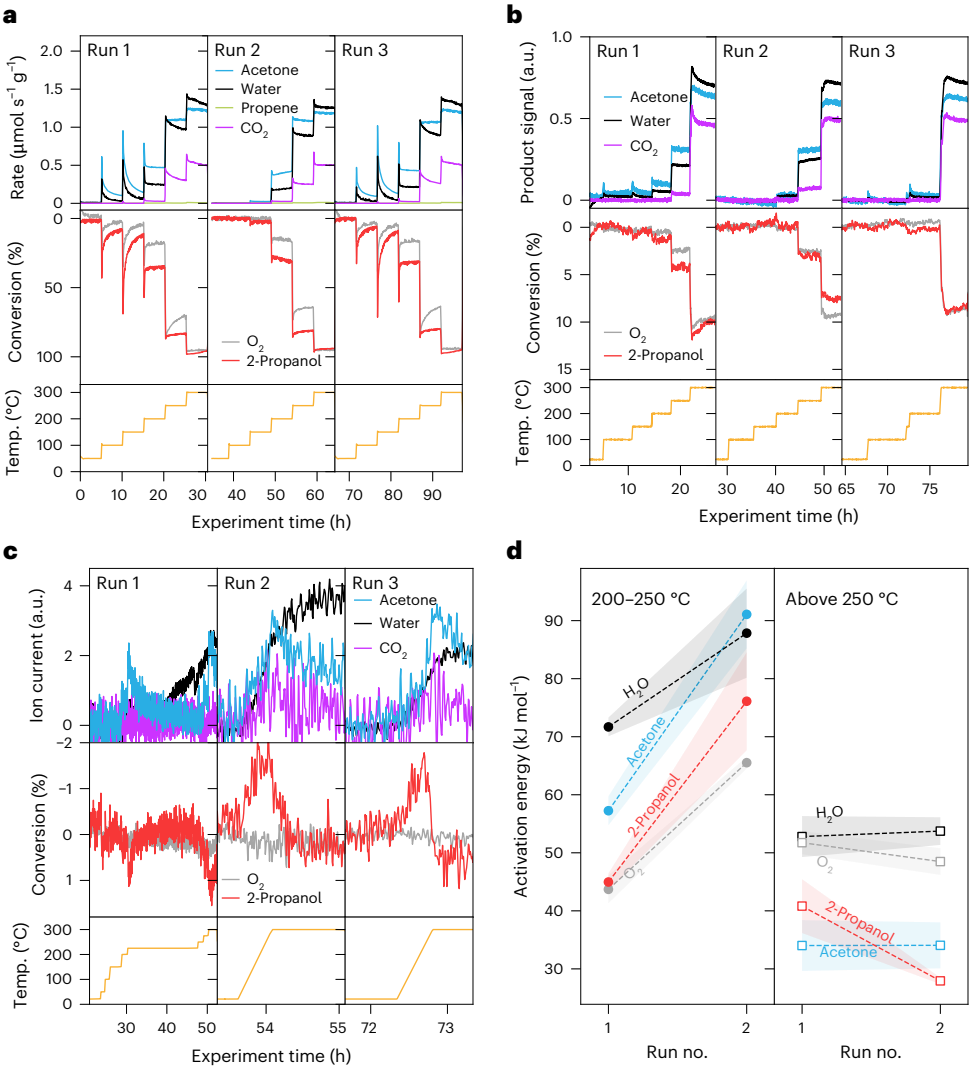

Fig. 2 | Activity. a–c, Catalytic data as obtained in a fixed-bed reactor (2 hPa 2-propanol, 2 hPa O_2, filled to 1,000 hPa with helium, measured by gas chromatography) (**a**), from operando NAP-XPS/NEXAFS experiments (0.25 hPa 2-propanol, 0.25 hPa O_2, measured by a QMS attached to the chamber via a leak valve) (**b**) and from an OTEM experiment (6.75 hPa 2-propanol, 6.75 hPa O_2, filled to 450 hPa with helium, measured using a QMS in the outlet stream of the nanoreactor) during the selective oxidation of 2-propanol (2-propanol/O_2 1:1) (**c**). The apparent negative conversions at low temperatures in the second and third run can be attributed to desorption of adsorbed 2-propanol (and to some extent acetone) in the nanoreactor. Note also that no substantial amount of propene is formed. **d**, Apparent activation energies for different products and reactants extracted from Arrhenius analyses of the activity in the NAP-XPS chamber (Supplementary Fig. 9). The dashed lines serve to guide the eye and the data points represent the Arrhenius fit parameters, while the shaded areas depict the s.d. as obtained from these fit parameters.

yield (TEY; Supplementary Figs. 25–27), this ratio appears to decrease linearly between 100 and 250 °C, similar to the oxidation state based on subsurface XPS spectra. It should be noted that these ratios are not independent of each other because a reduction of octahedral Co(III) to Co(II) changes not only the $Co^{III}_{oct}/Co^{II}_{oct}$ ratio, but also increases the relative amount of tetrahedral Co(II). Also, as seen in Supplementary Fig. 20, the spectrum of CoO features an intense resonance at 778.6 eV despite its octahedral coordination (Fig. 1b).

At room temperature, there is an accumulation of Co(II), in both tetrahedral and octahedral coordination, at the surface. This gets gradually oxidized towards a maximum oxidation state at 200 °C, coinciding with the transition from a low- to high-temperature activity regime (Fig. 2). This behaviour is seen for Co(II) in octahedral and tetrahedral sites, which both show the lowest occupancy at 200 °C. At higher temperatures, the surface is reduced again, which might explain the shift in reaction mechanism observed in the activation energies in Fig. 2d and the increased prominence of total oxidation as the increased amount of oxygen vacancies and reduced cobalt centres on the surface leads to altered adsorption properties and potentially to energetic shifts in the reaction pathways.

Morphology and crystallography

OTEM images of the identical location acquired at selected temperatures during the reaction are displayed in Fig. 4 (and in Supplementary Fig. 35 in greyscale). In Fig. 4a, two complete particles are visible, whereas Fig. 4b–d features enlarged regions from these overview images (see the marked rectangles in the room temperature image in Fig. 4a). The initial preoxidation step at 600 °C leads to smooth surfaces (Supplementary Figs. 36–39).

Even at room temperature in the reaction mixture (first row), nanometre-sized dark contrasts appear near the outer surface of the particles, as marked by the orange/white arrows. These features are around 2 nm in size (as shown in Supplementary Fig. 44) and are particularly noticeable at the top-left surface in Fig. 4b and around

https://doi.org/10.1038/s41929-025-01449-9

the perimeter of the small particle in Fig. 4d, but are also visible in Fig. 4c (top-right and bottom-left surfaces). Because these images are measured in transmission, it cannot be distinguished whether this contrast is due to nanoparticles sitting on top of the spinel grain, or due to changes in the bulk such as the accumulation of point defects/nucleating particles below the outer surfaces[28,29] as an initial stage of nanoparticle exsolution, which requires cation mobility towards the surface, a process that happens via interstitials in spinels[30,31]. Their exclusive proximity to the outer surfaces would suggest the latter because exsolution through the top facet would be expected to lead to a more homogeneous particle distribution. As the temperature is increased, particles ~3 nm (Supplementary Fig. 45) are exsolved from the outer surfaces (Supplementary Fig. 37 shows images at additional temperatures), indicating that the features at room temperature are indeed prestages of this process. Above 100 °C, the number and size of these particles does not increase any further (Supplementary Note 9, in particular Supplementary Figs. 45 and 46), suggesting that the exsolution is completed and that it is a self-limiting process. Although nanoparticle exsolution is a phenomenon most commonly observed in perovskite systems upon reduction, it has also been reported to occur for spinels[32–35].

Starting from 150 °C, moiré patterns emerge in the main particle (Fig. 4b; see Fig. 4a–d for images acquired at 200 °C), which can originate from either overlapping spinel crystallites with, for instance, slightly different degrees of reduction (and subsequently different lattice parameters)[36], or simply shifted/rotated lattices. Alternatively, they can originate from exsolved crystalline nanoparticles on top of the larger and much thicker (~60 nm; Supplementary Fig. 2) spinel grains. These might not be directly visible in mass-thickness contrast in the bright-field image, especially considering the strongly fluctuating diffraction contrast in the spinel itself.

Also at 150 °C, voids start forming in the bulk of the spinel particle (see in particular Fig. 4d and Supplementary Fig. 40). The cause of this is most probably the collapse of the vacancies created during the exsolution process. This hints at an increased cation mobility and is analogous to the (nanoscale) Kirkendall effect, which is also exhibited by cobalt upon oxidation[37]. Indeed, the Kirkendall effect was also demonstrated to occur for the synthesis of $Zn_xCo_{1-x}Co_2O_4$ nanocubes[30], where it was attributed to the high diffusivity of Co(II) ions inside the initially formed Co_3O_4 spinel. Raising the temperature beyond 200 °C causes a coalescence of these smaller voids into larger ones, which is also a typical process in systems exhibiting the Kirkendall effect[38]. Particularly noticeable in Fig. 4c, at 250 °C, the exsolved particles become more faceted, appearing cube-like.

In the second catalytic run (Supplementary Figs. 36 and 37), the morphology with the exsolved particles remains intact, whereas the system seems to be healed (that is, the voids refilled and the nanoparticles on the surface dissolved again) by the subsequent reoxidation treatment, leading again to a smooth surface that subsequently undergoes the same transformations and rearrangements in the third run. The same behaviour can be observed on all particles, some examples of which are given in Supplementary Figs. 38 and 39.

Because the exsolved particles are still present in the second run, yet the electronic structure behaves almost identically in all three runs, it can be inferred that the exsolution is a rare phenomenon. In fact, particularly in Fig. 4c, distinct cubic nanoparticles can be resolved, suggesting that there are not many particles overlapping along the viewing direction. This would equate to a nanoparticle coverage of at maximum ~7% (Supplementary Fig. 47), which is probably too low to be detectable in XPS, especially considering that Co_3O_4 already has contributions from Co(II) and Co(III).

In the selected-area electron diffraction (SAED) data from the first run in Fig. 5a (see Supplementary Fig. 41 for a linear representation), obtained under steady-state conditions between room temperature (blue) and 300 °C (red), most reflections can be attributed to the

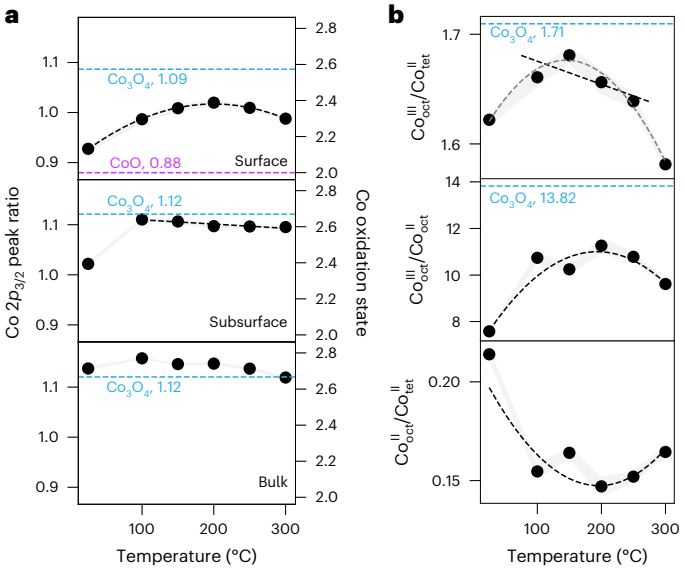

Fig. 3 | Electronic structure. a, Oxidation state analysis by cobalt $2p_{3/2}$ intensity ratios for kinetic energies of 150 eV (top, surface-sensitive), 600 eV (subsurface) and a photon energy of 4,900 eV (bottom, bulk-sensitive), as obtained from the NAP-XPS experiments. See Supplementary Fig. 18 for the respective spectra. Fully oxidized Co_3O_4 (blue dashed line) and CoO (purple dashed line) were used as reference data (Supplementary Fig. 20). **b**, Analysis of the intensity ratios of cobalt L_3-edge features (AEY, surface-sensitive, acquired in the same experiment as the NAP-XPS data) corresponding to tetrahedrally coordinated Co(II), octahedral Co(II) and octahedral Co(III). For TEY, refer to Supplementary Fig. 27. The dashed curves and lines correspond to parabolic or linear fits and serve to guide the eye and the grey-shaded regions denote the s.d. based on the noise level in the spectra (see also Supplementary Fig. 18) The data were acquired in a 1:1 mixture of 2-propanol and O_2 at a total pressure of 0.5 hPa.

Co_3O_4 spinel oxide[18]; however, starting from 225 °C, additional signals from rock-salt-type CoO emerge (Supplementary Table 5). These are highlighted by the grey backgrounds around 4.7 nm^{-1} and 6.65 nm^{-1}, corresponding to CoO 200 and 220 reflections, respectively[20], and grow in intensity with increasing temperature. High-resolution TEM (HRTEM) images were recorded during the operando experiment to locate these CoO crystals. An example is shown in Fig. 5b, obtained at 275 °C. The fast Fourier transform (FFT) of the exsolved particles (blue) reveals lattice spacings of 0.214 nm, agreeing well with CoO (200) lattice spacings[20], whereas the bulk only exhibits reflections stemming from the spinel (0.288 nm, corresponding to Co_3O_4 (220) planes). These assignments are both unambiguous because CoO does not feature any spacings at 0.288 nm, and Co_3O_4 does not feature any around 0.214 nm. At 50 °C, in contrast, where the exsolution has already started (Supplementary Figs. 36 and 37), the HRTEM image (Supplementary Fig. 42) shows no evidence of CoO, indicating that the exsolved particles are initially amorphous and crystallize at temperatures above 200 °C.

Spinel lattice parameters extracted from the SAED patterns (Fig. 5c; see Supplementary Note 10 for details on this procedure) show a severe non-linear behaviour below 200 °C. The lattice expands strongly up to 100 °C, then remains constant up until 200 °C, above which a linear behaviour is observed. In fact, fitting a linear function to the data points between 200 °C and 300 °C results in a line that coincides with the lattice parameter obtained at room temperature. The non-linearity can be attributed to lattice distortions resulting from the exsolution of cobalt ions and subsequent formation of cation vacancies: above 100 °C, the lattice parameter remains constant, which is in agreement with the stagnating number of exsolved particles at this temperature. Above 200 °C, coinciding with the transition in catalytic

https://doi.org/10.1038/s41929-025-01449-9

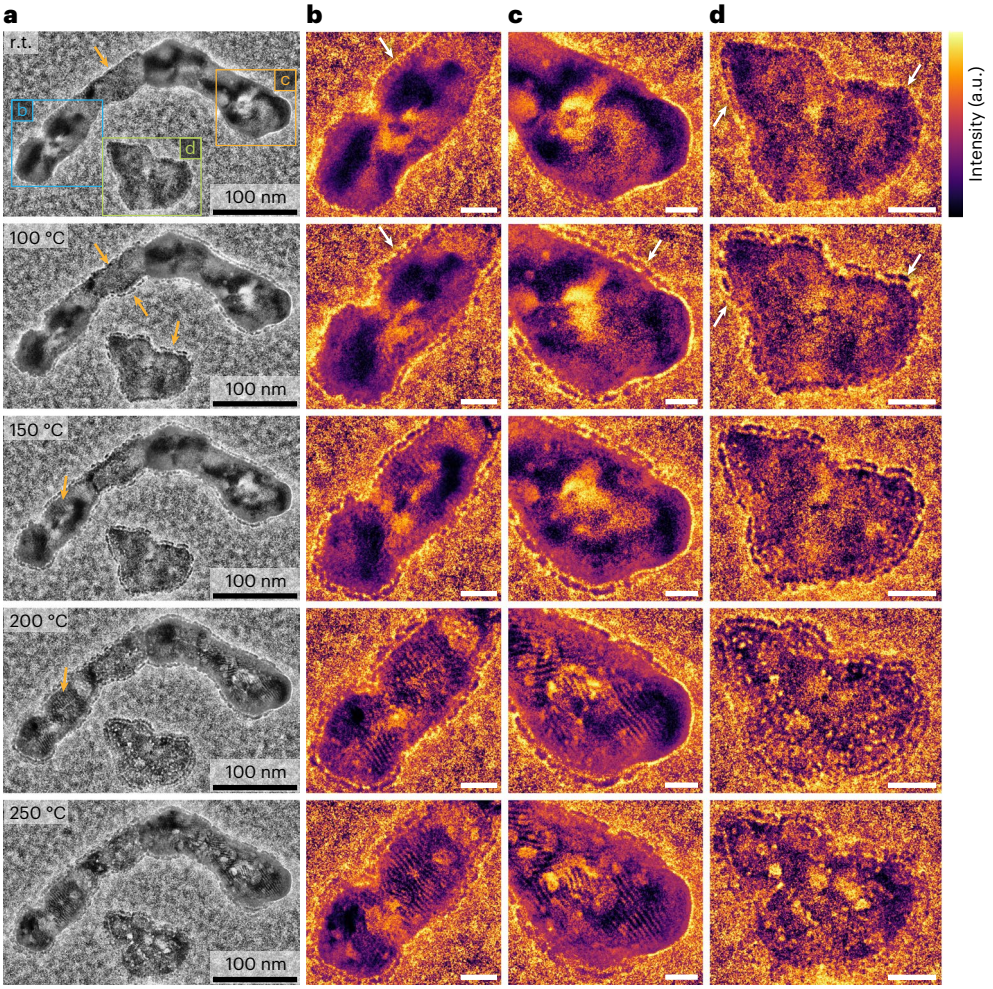

Fig. 4 | Morphology. a, Selected bright-field images from the OTEM experiments with enhanced contrast by local histogram equalization, acquired with an average electron dose rate of 51.8(6) $e\,nm^{-2}\,s^{-1}$ and an exposure of 1 s. **b**–**d**, Extracted and enlarged regions (marked by the blue (**b**), orange (**c**) and green (**d**) rectangles in the room temperature image in **a**) from the images, displayed in a different colour scheme (see colour bar in the first row) to improve the visibility of the formed voids and moiré patterns. Scale bars, 20 nm. The images were recorded in a 1:1 mixture of 2-propanol and O_2, with partial pressures of 6.75 hPa each, balanced to a total pressure of 450 hPa with helium. See Supplementary Fig. 35 for a greyscale representation.

behaviour from the low- to the high-temperature regime, the formation of voids inside the particles is observed, probably due to coalescence of vacancies, effectively restoring the non-defective spinel structure, leading to a linear thermal expansion behaviour again. In the second run, the initial lattice parameter at room temperature is significantly increased (due to oxygen vacancies), but the original value can be restored by reoxidation.

Discussion

Figure 6 presents a schematic overview of the bulk and surface solid-state processes of the Co_3O_4 catalyst during the reaction, along with a proposal for the underlying mechanisms at the atomic scale that can explain the phenomena observed in the operando experiments. During the preoxidation (Fig. 6a), the chemical potential of the gas phase ($\mu_{gas}(O_2)$) is equilibrated with the chemical potential of adsorbed oxygen species, μ_{ads}, and with the surface chemical potential of the fully oxidized, smooth spinel surface, $\mu_{surf.}$. Note that the chemical potential of the adsorbates on the surface is equal to the gas-phase chemical potential in equilibrium[39,40].

Upon introducing the reaction mixture (Fig. 6b), the difference in chemical potential between the gas phase (μ^{eff}_{gas}, for a 1:1 mixture of O_2/2-propanol; Supplementary Equation (3)) and the Co_3O_4 surface leads to a reduction-induced increase of cation mobility. This causes a subsurface accumulation of interstitial cobalt(II) ions ($Co_i^{\cdot\cdot}$), which have been reported to be the prevalent point defect at low oxygen partial pressures[41], and may serve as nucleation centres for the subsequently exsolved nanoparticles. In spinels, the tetrahedrally coordinated ions are presumed to be the mobile species by means of hopping between tetrahedral sites via the interstitial (vacant) octahedral site[30,31], and have been shown to be the exsolved species[33]. The high mobility in Co_3O_4 even at room temperature has recently been demonstrated by surface restructuring in ambient conditions[42]. In addition to surface reduction of Co(III), this interstitial accumulation serves as an additional origin of the increase in octahedrally coordinated Co(II) in the room temperature NEXAFS results. Ultimately, this process leads to the exsolution of amorphous Co(II) oxide nanoparticles at 50 °C, leaving behind cation vacancies at the tetrahedral sites in the spinel with a residual negative charge ($V''_{Co(t)}$). To compensate this residual charge, one possibility is that oxygen ions in the vicinity are oxidized to form O^- ions, which are suggested to exist for Co_3O_4 under electrochemical conditions at room temperature[43], and have, for instance, been reported to be formed thermally also in the subsurface of iridium oxides[44,45].

The number of exsolved particles and, thus, formed cation vacancies, increases up to 100 °C, and is accompanied by a strong increase in the spinel lattice parameter due to electrostatic repulsion between

https://doi.org/10.1038/s41929-025-01449-9

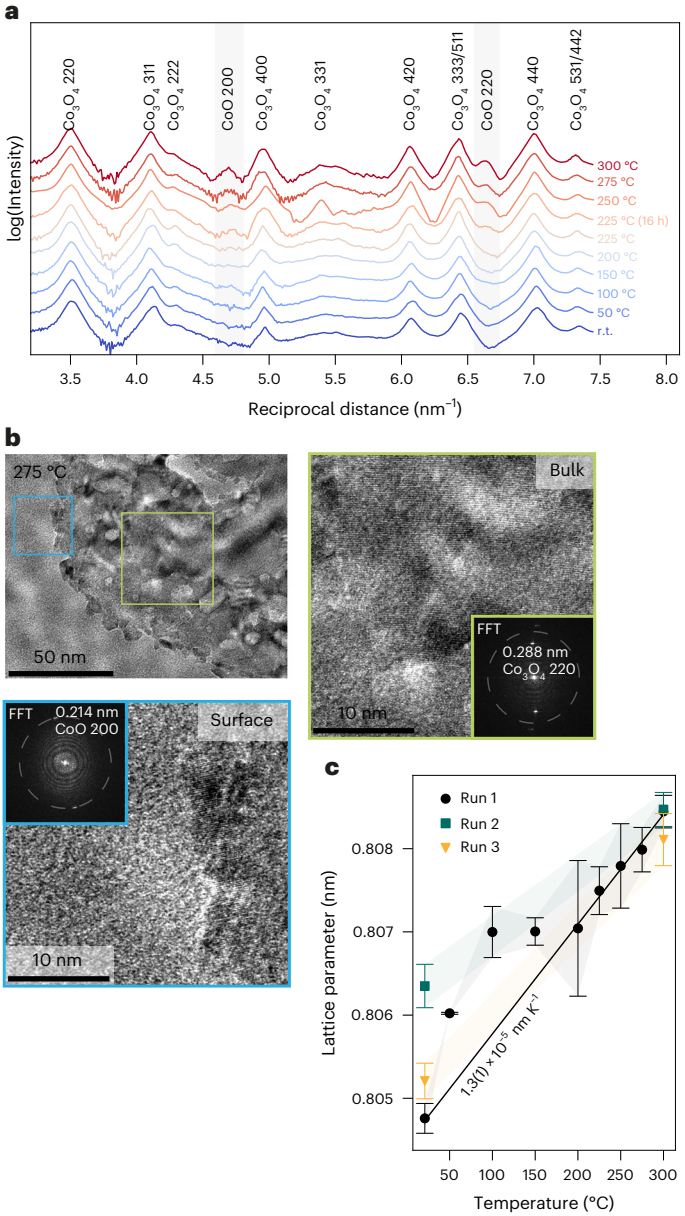

Fig. 5 | Crystallography. a, Steady-state SAED patterns (in logarithmic scale) reveal the formation of crystalline CoO above 225 °C (grey-shaded areas). **b**, HRTEM image acquired at 275 °C (dose rate, 4,500 e nm^{-2} s^{-1}; see Supplementary Note 8 for a study on beam damage) with two FFTs from the blue and green regions. At the surface, CoO (200) lattice spacings are visible, which are absent in the bulk (which shows Co_3O_4 planes instead). The dashed circle marks the CoO (200) lattice spacing in both FFTs to highlight its absence in the bulk. **c**, Co_3O_4 spinel lattice parameters extracted from steady-state SAED patterns. The line is a fit to the data from the first run above 200 °C, which coincides with the room temperature data point, but there is a strong deviation at lower temperatures. The shaded regions and error bars depict the s.d. obtained from fitting 30 peaks in three diffraction patterns per temperature (Supplementary Note 10). Reaction conditions were 2-propanol/O_2 1:1, 6.75 hPa partial pressures each, 450 hPa total pressure (balanced with helium).

these vacancies and the neighbouring oxygen anions (Fig. 6c). Above this temperature, both the number of exsolved particles and the lattice parameter remain constant (Supplementary Fig. 46). As observed in the OTEM images, the $V''_{Co(t)}$ cation (and correspondingly anion) vacancies start to collapse at 150 °C to form voids (Fig. 6d). As a result, the spinel structure with Co(II) at the tetrahedral sites and Co(III) at the octahedral sites is (to some extent) restored for the majority of unit cells, yielding a maximum in the surface oxidation state of cobalt. Consequently, large agglomerations of cation vacancies distorting the structure are no longer present. Hence, the lattice parameter exhibits linear behaviour again above 200 °C (Fig. 6e), where in addition the voids start to coalesce further to larger sizes. The observed lattice expansion is partially due to thermal expansion[46], but also due to the continuous formation of oxygen vacancies ($V_O^{\cdot\cdot}$) in this reductive environment (Fig. 3), with the average oxidation state decreasing above 200 °C (Fig. 6f).

As outlined in the beginning, the catalytic activity can be separated into a low-temperature and high-temperature region below and above 200 °C, respectively. In the low-temperature regime, the catalyst is comprised of a heavily defective spinel oxide with a strongly distorted lattice, decorated by amorphous, exsolved CoO_x nanoparticles. Cation vacancies have been suggested to improve electrocatalytic performance in the oxygen evolution reaction[47,48], which could also be the case in thermal oxidation reactions. What is changed in the second cycle, where this low-temperature activity is absent, is that the exsolved nanoparticles are already present and crystallized as CoO. Furthermore, although the spinel is still reduced at low temperatures and the cobalt oxidation state follows a parabolic behaviour (Supplementary Figs. 22 and 27), the lack of exsolution means that no $V''_{Co(t)}$ cation vacancies are formed, leading to a substantially lower concentration in the second run. This suggests that the low-temperature activity is associated with either the amorphous exsolved nanoparticles or the cation vacancies close to the surface (or even both), which implies the involvement of electrophilic oxygen in the low-temperature performance, which is line with oxygen K-edge measurements showing characteristic features for the existence of O^- species during oxidative activation (Supplementary Figs. 29 and 30, and Supplementary Note 6). In addition, the data also suggest that the reaction mechanism changes for temperatures above 200 °C, at which a Mars–van Krevelen mechanism is reported to be dominating[4,49]. This is in line with the extracted reaction pathways based on the product distribution (Supplementary Fig. 12 and Supplementary Note 3): at even higher temperatures (>250 °C), oxidative dehydrogenation, which can occur via the Mars–van Krevelen mechanism in contrast to dehydrogenation (which does not involve oxygen species), eventually becomes the prevalent reaction pathway, despite the cobalt oxidation state decreasing. The latter is probably the result of a secondary process, such as reduction by the hydrogen formed via dehydrogenation.

In the high-temperature activity regime, on the other hand, the catalyst is a less defective spinel, containing voids in the subsurface/bulk instead of the high cation defect concentration present in the low-temperature regime. The higher the temperature, the more reduced the surface becomes, and the more the gas-phase and adsorbate chemical potentials change due to the increased conversion of 2-propanol and oxygen and to increased total oxidation. Consequently, surface coverages also change, in turn affecting the measured apparent activation energies[50]. Nevertheless, below 250 °C, the apparent activation energies and the ratio between dehydrogenation and oxidative dehydrogenation change between first and second cycle (Fig. 2d and Supplementary Fig. 12), with oxidative dehydrogenation seemingly being more suppressed in the second run. This is most probably a result of the ongoing crystallization of CoO (Fig. 5) and void collapse to fewer, yet larger, voids (Fig. 4). In the second run, the voids no longer increase in volume (Supplementary Figs. 37 and 40), and they are dissolved during the reoxidation prior to the third run. This also leads to the dissolution of the exsolved particles (and the filling of the voids). In fact, nanoparticles exsolved from Co_3O_4 by reduction seem to be metastable: additional experiments (Supplementary Fig. 52) reveal that electrochemically exsolved nanoparticles are unstable when the sample is simply stored under ambient conditions. This is not only in line with the high mobility observed during the exsolution that is initiated in

https://doi.org/10.1038/s41929-025-01449-9

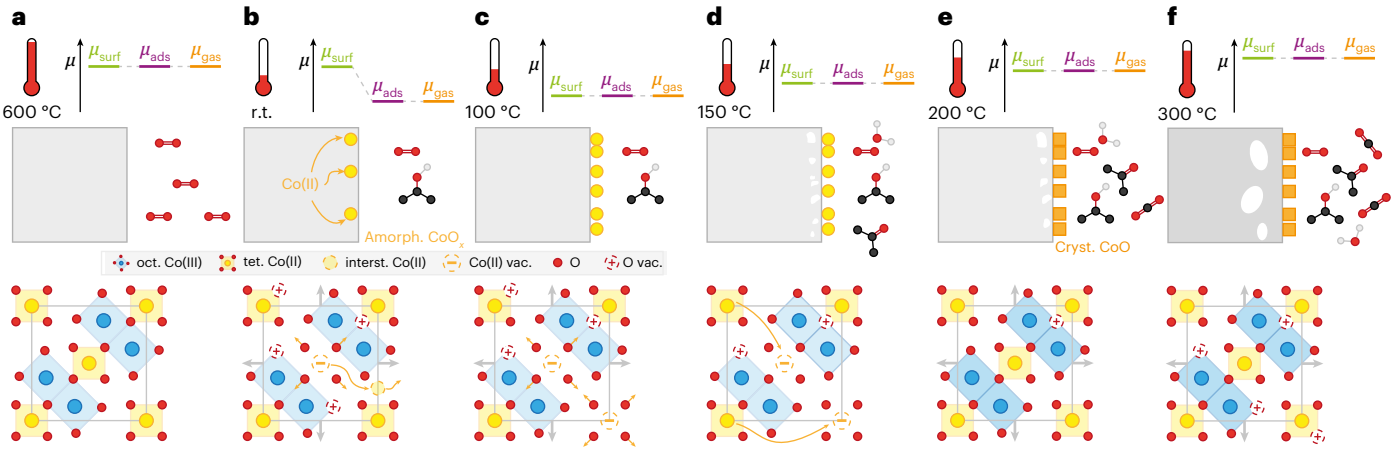

Fig. 6 | Scheme depicting the processes during the selective oxidation of 2-propanol on Co_3O_4. a–f, Schematic representation of the processes occuring on the Co_3O_4 catalyst during the preoxidation at 600 °C (**a**) and in reaction conditions at various temperatures from room temperature (**b**) up to 300 °C (**f**). Each grey square represents a Co_3O_4 particle; the energy diagram above it schematically shows the differences in chemical potential between surface and gas phase. Each lower image depicts the (bulk) spinel lattice in an atomically resolved picture in the [001] direction (only the first layers of tetragonal and octahedral sites are displayed for clarity). The colour coding is the same as in Fig. 1, with octahedrally coordinated Co(III) ions blue and tetrahedral Co(II) ions in yellow. Not shown in this scheme are oxidation state changes to accommodate vacancies. r.t., room temperature.

reaction feed at room temperature (see Fig. 4), but also with a recently reported surface restructuring of Co_3O_4 under ambient conditions[42].

The restoration of the undistorted spinel structure in the first run at 200 °C coincides with the start of the crystallization of CoO. Its reflections start appearing in the SAED patterns at 225 °C, where the coherence length is large enough to be detected by diffraction techniques, but initial nucleation can be expected to start even at lower temperatures. Thus, at 200 °C, which is the temperature with the highest selectivity towards acetone (Supplementary Fig. 8) and the transition between the low- and high-temperature regime, the catalyst can be conceived to be in a metastable state or even trapped in a frustrated phase transition[51]. When frustrated, the catalyst is energetically excited and in the transition between two energetically equivalent states, where small changes to the conditions can cause the system to flip between these states. This frustrated state is often associated with improved activity or selectivity[52,53]. In this case, with the exsolved, amorphous particles starting to crystallize, the vacancies in the spinel collapsing into the voids as seen in the bright-field images, and additionally, the cobalt oxidation state reaching a maximum, there are multiple processes confining the spinel catalyst to this frustrated state between a defective spinel decorated with amorphous CoO_x particles (exhibiting quick deactivation) and a restored, void-containing spinel with crystalline CoO nanoparticles (yielding stable conversion), as detailed in Supplementary Fig. 17.

In summary, substantial dynamics are at play during the oxidation of 2-propanol on Co_3O_4, turning the surface into a dynamic entity affected by diffusional solid-state processes. The catalytic activity is affected by strong restructuring due to exsolution of reduced CoO_x nanoparticles, thus effectively forming the catalyst, and changing cation and anion vacancy concentrations leading up to their coalescence to form voids in the subsurface. All of these will also have electronic influences in the adsorption of reactants and products alike, with these subsurface/bulk processes effectively controlling the reactivity. As outlined above, the ideal combination of activity and selectivity is found when the catalyst is trapped in the transition between the more transient low-temperature regime and the stationary high-temperature regime. Thus, it is desirable to keep the catalyst in this potentially frustrated state for optimized performance. This can be achieved by maintaining optimal working conditions, but might also be further enhanced by catalyst design and suitable pretreatment, such as laser treatment to introduce defects[47,48].

Methods

Operando NAP-XAS/XPS

The soft and tender X-ray branches of the EMIL beamline (UE48-PGM and CPMU17-DCM) at the BESSY II electron storage ring were used for synchrotron-based XAS (more accurately NEXAFS) and XPS measurements at the CAT end-station. Both branches are focused on the same spot on the sample and allow for seamless switching between soft and tender X-ray beams during the experiment[54].

The soft X-ray beamline was operated with a monochromator equipped with an 800 lines mm^{-1} grating and an exit slit of 10 µm, resulting in nominal band widths of 60 meV and 100 meV for oxygen K and cobalt L edges, respectively. A differentially pumped Specs Phoibos 150 NAP hemispherical analyser, coupled to a two-dimensional delay line detector, was used to detect photoelectrons with a pass energy of 10 eV. During NEXAFS, TEY measurements were conducted by collecting the drain current at the entrance aperture of the spectrometer, which was biased to 90 V to remove gas-phase contributions. Simultaneously, the electron analyser was used to record AEY, with kinetic energies of 615 eV and 335 eV for the cobalt L and oxygen K edges, respectively. The kinetic energies were chosen such that there is no overlap of a photoemission core level peak with the measurement window, and the most intense Auger transitions (Co-LMM and O-KLL) were not used to avoid the valence bands.

Tender XPS and XANES spectroscopy in the tender range were acquired using the double-crystal monochromator of the CPMU17 branch (equipped with a Si(111) crystal pair). For XANES, it was operated in channel-cut mode, and, as signals, TEY and AEY (at the Co-LMM maximum at 773.6 eV) were acquired, providing notable differences in signal depths (nominally 1.6 nm for AEY, compared to more than 300 nm for TEY; see also Supplementary Table 4 and Supplementary Fig. 28, including the discussion in Supplementary Note 10). All cobalt K edges were normalized to I_0 using a gold mesh in the beamline. They were shift-corrected using the monochromator glitches present in the raw (unnormalized) data, and then calibrated to literature values based on the edge position (Supplementary Fig. 33) of the fully oxidized sample[43].

For photoelectron spectra, potential offsets from the monochromator were corrected for by the valence band (inflection point), which was recorded at every photon energy and, additionally at $h\nu = 150$ eV, where any offset from the monochromator is negligibly small.

For cobalt 2*p* spectra, any additional residual shifts (for example, from the lens system) were removed by cross-correlation of the spectra. All shift-correction measures were additionally cross-checked with the carbon 1*s* binding energies of the C–C component (at 284.8 eV). The cobalt oxidation state was determined by measuring intensity ratios as shown in Supplementary Figs. 18 and 25. Synthetic spectra were generated by a linear combination of Co_3O_4 and CoO cobalt 2*p* reference spectra (Supplementary Fig. 20) to determine the relation between the respective intensity ratios and the cobalt oxidation state, as shown in Supplementary Fig. 21. The standard deviation was estimated by the noise level in the low-binding-energy region (XPS) or pre-edge (NEXAFS) spectra, as shown in Supplementary Fig. 18.

A chamber pressure of 0.5 hPa was used. Product detection was accomplished by a differentially pumped Pfeiffer Prisma Pro quadrupole mass spectrometer (QMS) connected to the main chamber via a leak valve. The QMS signal intensity was calibrated to the gas amount in the chamber using a multipoint calibration with 3–5 different partial pressures for each reactant and product gas. For oxidation steps, the chamber was filled with pure oxygen, while, for reactions, 1:1 mixtures of 2-propanol vapour (dosed via a low-Δp mass-flow controller, Bronkhorst) and O_2 were used (flows of 2 ml min^{-1} each, resulting in partial pressures of 0.25 hPa each), which were additionally mixed with a small flow of argon (0.2 ml min^{-1}) to normalize changes over time in the QMS pressure. The sample was pelletized (8 mm diameter, ~15 mg) and mounted in a sapphire sample holder. During the reaction, the sample was heated from the back using a near-infrared laser. The temperature was measured with a K-type thermocouple (mounted on the spectrometer-facing side of the pellet) and kept constant using a Eurotherm PID controller.

OTEM

OTEM was conducted using an image-corrected ThermoFisher Scientific Titan 80-300 instrument operated at 300 keV and equipped with a Gatan Imaging Filter (GIF) Tridiem and a TVIPS TemCam-XF 416R CMOS camera.

A DENSsolutions climate in situ holder was used for the operando studies. Bottom and top chips of the nanoreactor were plasma cleaned using a low-energy O_2/Ar plasma prior to sample deposition. The latter was achieved by drop-casting 1.5 µl of a sonicated suspension of Co_3O_4 in anhydrous ethanol (5 mg ml^{-1}) onto the heating spiral of the heating chip under an optical microscope, resulting in a nominal loading of around 7.5 µg of Co_3O_4. After assembly, the whole holder was plasma cleaned in a slightly more aggressive O_2/Ar plasma to minimize carbon build-up on the vacuum side of the chips during the long-running experiments.

The holder was attached to a home-built gas-feeding system[55], modified to accommodate a double-walled gas saturator to enable use of 2-propanol vapour. For reaction conditions, pure helium was flowed through a double-walled glass saturator filled with water-free 2-propanol (VWR Chemicals, ≥99.8%, max. 0.003% H_2O) and kept at 10 °C for a controlled vapour pressure of 22.5 hPa. The helium flow was controlled by a mass-flow controller (Bronkhorst) and set to 22 ml min^{-1}, which was mixed with a flow of 0.5 ml min^{-1} of O_2 and kept at a constant pressure of 1,500 hPa using a back-pressure controller. Via a leak valve, a fraction of this flow was pumped through the holder (~13 µl min^{-1}, leading to an inlet pressure of 900 hPa at the DENSsolutions climate holder). This leads to partial pressures of 6.75 hPa for both 2-propanol and O_2, and a total pressure of around 450 hPa in the nanoreactor. For conversion detection, the total flow through the sample holder was directed to a Hiden HAL/3F RC triple-filter QMS. Pre- and reoxidation conditions were obtained by mixing 2 ml min^{-1} O_2 and 8 ml min^{-1} of helium (see also Supplementary Fig. 5 and Supplementary Table 1).

For all images, the electron dose rate was chosen such that no beam damage could be observed. Beam damage studies are presented in Supplementary Fig. 43.

OTEM data analysis. For the comparison of particle shapes, different bright-field images of the same particles were aligned using template matching. SAED patterns were processed using Python scripts. A modification of Fritsch et al.'s centre-finding and distortion-correction algorithm was applied[56]. Subsequently, a distortion correction based on polar transforms and aberration correction was applied, as detailed in Supplementary Note 10. Reflections of Co_3O_4 were peak-fitted using Voigt profiles and subsequently, the lattice parameter was obtained from all fitted reflexes at each temperatures, with outliers removed using *z*-score-based filtering[57]. More details on this procedure are given in Supplementary Figs. 48–51 in Supplementary Note 10.

General characterization

Ex situ scanning transmission electron microscopy characterization of the as-synthesized Co_3O_4 catalyst was conducted using a double-corrected Jeol JEM-ARM200F equipped with a cold field emission gun. The platelet thickness distribution was obtained by computing a kernel density estimation (Supplementary Fig. 3)[58].

The X-ray diffraction (XRD) measurements were performed in Bragg–Brentano geometry on a Bruker AXS D8 Advance A25 theta/theta diffractometer, using copper $K\alpha_{1+2}$ radiation and a position-sensitive energy-dispersive LynxEye XE-T silicon strip detector in high-energy resolution mode (no nickel filter required). The sample powder was filled into the cavity of a low background silicon single-crystal sample holder, the surface of the powder bed being level with the sample holder edge (front loading). XRD patterns were recorded in continuous scanning mode in the range of 5–135° 2θ with increments of 0.02° and a counting time of 1 s per step, resulting in a total accumulation time of 192 s per data point.

Reactor measurements

The reactor measurements were performed in a home-built set-up described elsewhere[59]. The measurement set-up is equipped with a HovaGAS N G6 VOC-S liquid and gas dosing system (IAS). The dosing system consists of six lines, each of which is controlled by a thermal high-precision mass-flow controller (Bronkhorst). Water and/or an organic solvent can be added to the carrier gas (N_2) via two parallel saturators. Afterwards, all the gases are mixed in a cross-piece at 110 °C. The gas is then mixed with water and/or an organic solvent, and is fed through heated tubes into a U-shaped fixed-bed reactor made of Duran or quartz glass with an inner diameter of 8 mm before the catalyst bed and 4 mm at the outlet. In this reactor, 100 mg of Co_3O_4 catalyst (sieve fraction, 250–355 µm) was placed on a quartz wool support, which resulted in a bed length of 2.2 mm. A type-K thermocouple is used to measure the temperature inside this reactor bed. The reactor is placed in a tube furnace, allowing temperatures of up to 1,000 °C to be reached. The reactor and tube furnace are additionally placed in a heated cabinet (Salvislab Thermocenter TC100). The gas can either run through the reactor or bypass it. The reactor outlet stream is analysed by a downstream four-channel micro gas chromatograph (Fusion Micro GC, Inficon) via four columns (2 × Rt-Molsieve 5A (1 × He, 1 × Ar), 1 × Stabilwax DB (He), 1 × Rt-Q-Bond (He)). In the end, the gas runs through a gas wash bottle and is then discharged into the exhaust air. The lines have a diameter of 1/8 inch and are made of stainless steel except for tubes inside the heating cabinet between the four-way valve and the reactor (1/16 inch).

In a first step, the operando protocol was followed (Supplementary Fig. 5). The catalyst was heated to 600 °C (5 K min^{-1}) in 20% O_2 (Westfalen, 20.5 vol% O_2 in N_2, <0.1 ppm hydrocarbons) in N_2 (evaporated from liquid nitrogen (Air Liquide) and filtered by an SGT triple filter (moisture/hydrocarbons/CO_2)) with a flow of 50 ml min^{-1}. This temperature was held for 3 h before cooling down to 50 °C. After purging the reactor for 20 min with 100 ml min^{-1} N_2 and 45 min with reaction mixture (0.18% 2-propanol (Fischer Chemical, >99.9%) and 0.18% O_2 in N_2; total flow, 100 ml min^{-1}), the temperature steps were started by consecutively

heating the catalyst to 300 °C in 50 °C steps (10 K min^{-1}) and keeping each temperature for 5 h (first run). The system was subsequently cooled down to 50 °C and the temperature steps repeated (second run). Afterwards, a reoxidation at 600 °C was performed as in the operando experiments, followed by a third run of the temperature steps.

To investigate the stability of the catalyst, the catalyst was afterwards again reoxidized at 600 °C. After purging with N_2, the catalyst was heated to 250 °C (5 K min^{-1}) in the reaction mixture and held at this temperature for 44 h.

Sample synthesis

The synthesis of the Co_3O_4 platelets was conducted in an automatic lab reactor system (OptiMax 1001, Mettler Toledo)[60]. A $Co(OH)_2$ precursor was precipitated by dosing 125 g of a 0.8 M $Co(NO_3)_2{\cdot}6H_2O$ (≥98%, Carl Roth) solution continuously over 1 h at 50 °C into a reactor, prefilled with 200 ml distilled water. A constant pH of 8.5 was ensured by simultaneously dosing 0.6 M NaOH (98.5%, VWR) as precipitation agent.

Following precipitation, the material was aged for 1 h without pH control at 50 °C. During the reaction, the reactor was continuously purged with N_2 and stirred at 350 r.p.m. After cooling to room temperature, the precipitated $Co(OH)_2$ precursor was washed with water several times and dried at room temperature in vacuum. Subsequently, the dried precursor was calcined at 300 °C (2 K min^{-1}) for 3 h in a muffle furnace (Nabertherm LE 6/11/B150).

The resulting hexagonal platelets with thicknesses of around 60 nm (Supplementary Figs. 2 and 3) were shown to be phase pure by Rietveld fitting of the XRD data (Supplementary Fig. 4).

Data availability

The raw data supporting the findings of this study are publicly available at the AC/CATLAB archive via https://ac.archive.fhi.mpg.de/D63268 or from the corresponding authors.

References

1. Ertl, G., Knözinger, H., Schüth, F. & Weitkamp, J. (eds) *Handbook of Heterogeneous Catalysis* (Wiley-VCH, 2008).
2. Najafishirtari, S. et al. A perspective on heterogeneous catalysts for the selective oxidation of alcohols. *Chem. Eur. J.* **27**, 16809–16833 (2021).
3. Mallat, T. & Baiker, A. *Oxidation of Alcohols with Molecular Oxygen* in *Handbook of Heterogeneous Catalysis* 1st edn (eds Ertl, G., et al.) 3521–3538 (Wiley-VCH, 2008).
4. Anke, S. et al. Selective 2-propanol oxidation over unsupported Co_3O_4 spinel nanoparticles: mechanistic insights into aerobic oxidation of alcohols. *ACS Catalysis* **9**, 5974–5985 (2019).
5. Zhang, H. et al. A resource utilization method for volatile organic compounds emission from the semiconductor industry: selective catalytic oxidation of isopropanol to acetone over Au/α-Fe_2O_3 nanosheets. *Appl. Catal. B* **275**, 119011 (2020).
6. Teng, Y., Song, L. X., Wang, L. B. & Xia, J. Face-raised octahedral Co_3O_4 nanocrystals and their catalytic activity in the selective oxidation of alcohols. *J. Phys. Chem. C* **118**, 4767–4773 (2014).
7. Jagadeesh, R. V. et al. Selective oxidation of alcohols to esters using heterogeneous Co_3O_4–N@C catalysts under mild conditions. *J. Am. Chem. Soc.* **135**, 10776–10782 (2013).
8. Gopinath, S. et al. Improved catalytic performance of cobalt oxide for selective oxidation of benzyl alcohol. *SN Appl. Sci.* **1**, 520 (2019).
9. Rodrigues, C. P., Da Silva, V. T. & Schmal, M. Partial oxidation of ethanol over cobalt oxide based cordierite monolith catalyst. *Appl. Catal. B* **96**, 1–9 (2010).
10. Nie, R. et al. A sandwich N-doped graphene/Co_3O_4 hybrid: an efficient catalyst for selective oxidation of olefins and alcohols. *J. Mater. Chem. A* **1**, 9037 (2013).
11. Meirer, F. & Weckhuysen, B. M. Spatial and temporal exploration of heterogeneous catalysts with synchrotron radiation. *Nat. Rev. Mater.* **3**, 324–340 (2018).
12. Bañares, M. A. & Wachs, I. E. Molecular structures of supported metal oxide catalysts under different environments: molecular structures of supported metal oxide catalysts. *J. Raman Spectrosc.* **33**, 359–380 (2002).
13. Somorjai, G. New model catalysts (platinum nanoparticles) and new techniques (SFG and STM) for studies of reaction intermediates and surface restructuring at high pressures during catalytic reactions. *Appl. Surf. Sci.* **121–122**, 1–19 (1997).
14. Rupprechter, G. & Freund, H.-J. Adsorbate-induced restructuring and pressure-dependent adsorption on metal nanoparticles studied by electron microscopy and sum frequency generation spectroscopy. *Top. Catal.* **14**, 3–14 (2000).
15. Köpfle, N. et al. Zirconium-assisted activation of palladium to boost syngas production by methane dry reforming. *Angew. Chem. Int. Ed.* **57**, 14613–14618 (2018).
16. Pan, C.-J. et al. Tuning/exploiting strong metal–support interaction (SMSI) in heterogeneous catalysis. *J. Taiwan Inst. Chem. Eng.* **74**, 154–186 (2017).
17. Chee, S. W., Lunkenbein, T., Schlögl, R. & Roldán Cuenya, B. Operando electron microscopy of catalysts: the missing cornerstone in heterogeneous catalysis research? *Chem. Rev.* **123**, 13374–13418 (2023).
18. Picard, J., Baud, G., Besse, J. & Chevalier, R. Croissance cristalline et étude structurale de Co_3O_4. *J. Less Common Metals* **75**, 99–104 (1980).
19. Sickafus, K. E., Wills, J. M. & Grimes, N. W. Structure of spinel. *J. Am. Ceram. Soc.* **82**, 3279–3292 (1999).
20. Sasaki, S., Fujino, K. & Takéuchi, Y. X-ray determination of electron-density distributions in oxides, MgO, MnO, CoO, and NiO, and atomic scattering factors of their constituent atoms. *Proc. Jpn. Acad. B* **55**, 43–48 (1979).
21. Raveau, B. & Seikh, M. M. *Cobalt Oxides: From Crystal Chemistry to Physics* 1st edn (Wiley, 2012).
22. Gervasini, A. Acidity and basicity of metal oxide surfaces II. Determination by catalytic decomposition of isopropanol. *J. Catal.* **131**, 190–198 (1991).
23. Dai, W. & Ren, L. *Dehydrogenation of Alcohols: Formaldehyde* in *Handbook of Heterogeneous Catalysis* 1st edn (eds Ertl, G. et al.), 3256–3265 (Wiley, 2008).
24. Petitto, S. C., Marsh, E. M., Carson, G. A. & Langell, M. A. Cobalt oxide surface chemistry: the interaction of CoO(100), Co_3O_4(110) and Co_3O_4(111) with oxygen and water. *J. Mol. Catal. A* **281**, 49–58 (2008).
25. Chen, J., Wu, X. & Selloni, A. Electronic structure and bonding properties of cobalt oxide in the spinel structure. *Phys. Rev. B* **83**, 245204 (2011).
26. Kim, K. J. & Park, Y. R. Optical investigation of charge-transfer transitions in spinel Co_3O_4. *Solid State Commun.* **127**, 25–28 (2003).
27. Bergmann, A. et al. Unified structural motifs of the catalytically active state of Co(oxyhydr)oxides during the electrochemical oxygen evolution reaction. *Nat. Catal.* **1**, 711–719 (2018).
28. Williams, D. B. & Carter, C. B. *Transmission Electron Microscopy: A Textbook for Materials Science* 2nd edn (Springer, 2009).
29. Shi, C. *Characterization and Simulation of p-Type Ion Implantation in MCT* in *Ion Beam Applications* 1st edn (eds Ahmad, I. & Maaza, M.), 161–178 (InTech, 2018).
30. Tian, L. et al. Hollow single-crystal spinel nanocubes: the case of zinc cobalt oxide grown by a unique Kirkendall effect. *Inorg. Chem.* **47**, 5522–5524 (2008).
31. Sotoudeh, M., Dillenz, M. & Groß, A. Mechanism of magnesium transport in spinel chalcogenides. *Adv. Energy Sustain. Res.* **2**, 2100113 (2021).

32. Zhang, J., Gao, M.-R. & Luo, J.-L. In situ exsolved metal nanoparticles: a smart approach for optimization of catalysts. *Chem. Mater.* **32**, 5424–5441 (2020).
33. Cho, E. et al. Ni catalysts for dry methane reforming prepared by A-site exsolution on mesoporous defect spinel magnesium aluminate. *Appl. Catal. A* **602**, 117694 (2020).
34. Guo, X. et al. An exsolution constructed FeNi/$NiFe_2O_4$ composite: preferential breaking of octahedral metal–oxygen bonds in a spinel oxide. *Chem. Sci.* **13**, 9440–9449 (2022).
35. Wong, Y. J. et al. Development of Co supported on Co–Al spinel catalysts from exsolution of amorphous Co–Al oxides for carbon dioxide reforming of methane. *ChemCatChem* **11**, 5593–5605 (2019).
36. Ostyn, K. & Carter, C. On the reduction of nickel oxide. *Surf. Sci.* **121**, 360–374 (1982).
37. Yin, Y. et al. Formation of hollow nanocrystals through the nanoscale Kirkendall effect. *Science* **304**, 711–714 (2004).
38. Railsback, J. G., Johnston-Peck, A. C., Wang, J. & Tracy, J. B. Size-dependent nanoscale Kirkendall effect during the oxidation of nickel nanoparticles. *ACS Nano* **4**, 1913–1920 (2010).
39. Trinh, T., Bedeaux, D., Simon, J.-M. & Kjelstrup, S. Calculation of the chemical potential and the activity coefficient of two layers of CO_2 adsorbed on a graphite surface. *Phys. Chem. Chem. Phys.* **17**, 1226–1233 (2015).
40. Alfè, D. & Gillan, M. J. Ab Initio statistical mechanics of surface adsorption and desorption. I. H_2O on MgO (001) at low coverage. *J. Chem. Phys.* **127**, 114709 (2007).
41. Kaczmarska, A., Grzesik, Z. & Mrowec, S. On the defect structure and transport properties of Co_3O_4 spinel oxide. *High Temp. Mater. Processes* **31**, 371–379 (2012).
42. Schmidt, F.-P. et al. Subnanometer tracking of the oxidation state on Co_3O_4 nanoparticles by identical location imaging and spectroscopy. *ACS Appl. Mater. Interfaces* **17**, 9419–9430 (2025).
43. Haase, F. T. et al. Size effects and active state formation of cobalt oxide nanoparticles during the oxygen evolution reaction. *Nat. Energy* **7**, 765–773 (2022).
44. Pfeifer, V. et al. Reactive oxygen species in iridium-based OER catalysts. *Chem. Sci.* **7**, 6791–6795 (2016).
45. Carbonio, E. A. et al. Thermal synthesis of electron deficient oxygen species on crystalline IrO_2. *Catal. Sci. Technol.* 10.1039.D3CY01026K (2024).
46. Broemme, A. Correlation between thermal expansion and Seebeck coefficient in polycrystalline Co_3O_4. *IEEE Trans. Elect. Insul.* **26**, 49–52 (1991).
47. Lu, Y. et al. Engineering of cation and anion vacancies in Co_3O_4 thin nanosheets by laser irradiation for more advancement of oxygen evolution reaction. *Nano Energy* **83**, 105800 (2021).
48. Liu, W., Kamiko, M., Yamada, I. & Yagi, S. Effects of cation vacancies at tetrahedral sites in cobalt spinel oxides on oxygen evolution catalysis. *Mater. Adv.* **3**, 7513–7519 (2022).
49. Finocchio, E., Willey, R. J., Busca, G. & Lorenzelli, V. FTIR studies on the selective oxidation and combustion of light hydrocarbons at metal oxide surfaces. Part 3—Comparison of the oxidation of C_3 organic compounds over Co_3O_4, $MgCr_2O_4$ and CuO. *Faraday Trans.* **93**, 175–180 (1997).
50. Teschner, D. et al. In situ surface coverage analysis of RuO_2-catalysed HCl oxidation reveals the entropic origin of compensation in heterogeneous catalysis. *Nat. Chem.* **4**, 739–745 (2012).
51. Schlögl, R. Heterogeneous catalysis. *Angew. Chem. Int. Ed.* **54**, 3465–3520 (2015).
52. Greiner, M. T., Jones, T. E., Klyushin, A., Knop-Gericke, A. & Schlögl, R. Ethylene epoxidation at the phase transition of copper oxides. *J. Am. Chem. Soc.* **139**, 11825–11832 (2017).
53. Cao, J. et al. In situ observation of oscillatory redox dynamics of copper. *Nat. Commun.* **11**, 3554 (2020).
54. Hendel, S. et al. The EMIL project at BESSY II: beamline design and performance. *AIP Conf. Proc.* **1741**, 030038 (2016).
55. Plodinec, M. et al. Versatile homebuilt gas feed and analysis system for operando TEM of catalysts at work. *Microsc. Microanal.* **26**, 220–228 (2020).
56. Fritsch, B. et al. Sub-Kelvin thermometry for evaluating the local temperature stability within in situ TEM gas cells. *Ultramicroscopy* **235**, 113494 (2022).
57. Virtanen, P. et al. SciPy 1.0: fundamental algorithms for scientific computing in Python. *Nat. Methods* **17**, 261–272 (2020).
58. Pedregosa, F. et al. Scikit-learn: machine learning in Python. *J. Mach. Learn. Res.* **12**, 2825–2830 (2011).
59. Dreyer, M. et al. Beneficial effects of low iron contents on cobalt-containing spinel catalysts in the gas phase 2-propanol oxidation. *ChemCatChem* **14**, e202200472 (2022).
60. Rabe, A. et al. The roles of composition and mesostructure of cobalt-based spinel catalysts in oxygen evolution reactions. *Chem. Eur. J.* **27**, 17038–17048 (2021).

Acknowledgements

This work was funded by the Deutsche Forschungsgemeinschaft (DFG, German Research Foundation), 388390466–TRR 247. T.G., D.C. and T.L. additionally acknowledge funding by the Federal Ministry of Education and Research in the framework of the project Catlab (03EW0015B). The authors thank the Helmholtz-Zentrum Berlin für Materialien und Energie for the allocation of synchrotron radiation beamtime at the UE48-PGM and U17-DCM beamlines at EMIL.

Author contributions

T.G., A.K.-G. and T.L. planned the experiments and wrote the manuscript. T.G. performed the operando NAP-XPS/NEXAFS investigations with help from D.C., P.Z., A.E., M.G. and M.H. T.G. conducted the operando TEM experiments. T.G. performed data analysis and interpretation. F.G. and J.A. did the XRD experiments and the analysis thereof. A.K.-G. and T.L. contributed to discussions and interpretation. A.R., M.D., N.C. and S.N. synthesized and characterized the powder sample and performed catalytic tests. R.S., M.B. and T.L. initiated the project and provided funding and perspectives.

Funding

Open access funding provided by Max Planck Society.

Competing interests

The authors declare no competing interests.

Additional information

Supplementary information The online version contains supplementary material available at https://doi.org/10.1038/s41929-025-01449-9.

Correspondence and requests for materials should be addressed to Thomas Götsch or Thomas Lunkenbein.

Peer review information *Nature Catalysis* thanks Patricia Kooyman and the other, anonymous, reviewer(s) for their contribution to the peer review of this work.

[1]Fritz-Haber-Institut der Max-Planck-Gesellschaft, Department of Inorganic Chemistry, Berlin, Germany. [2]Helmholtz-Zentrum Berlin für Materialien und Energie GmbH, Chemical Energy Division, Berlin, Germany. [3]Christian-Albrechts-Universität zu Kiel, Institute of Inorganic Chemistry, Kiel, Germany. [4]Universität Duisburg-Essen, Faculty of Chemistry and Center for Nanointegration Duisburg-Essen (CENIDE), Essen, Germany. [5]Max Planck Institute for Chemical Energy Conversion, Department of Heterogeneous Reactions, Mülheim an der Ruhr, Germany. [6]Helmholtz-Zentrum Berlin für Materialien und Energie GmbH, Interface Design, Berlin, Germany. [7]Helmholtz-Zentrum Berlin für Materialien und Energie GmbH, Energy Materials In-situ Laboratory Berlin (EMIL), Berlin, Germany. [8]Present address: University of Bayreuth, Bavarian Center for Battery Technology (BayBatt), Bayreuth, Germany. [9]Present address: University of Bayreuth, Chair of Operando-Analytics for Electrochemical Energy Storage, Bayreuth, Germany. ✉e-mail: goetsch@fhi-berlin.mpg.de; lunkenbein@fhi-berlin.mpg.de